Contents lists available at ScienceDirect

Analytica Chimica Acta

journal homepage: www.elsevier.com/locate/aca

Pt,P-codoped carbon nitride nanoenzymes for fluorescence and colorimetric dual-mode detection of cholesterol

Meiling Chen [a,1], Yang Yang [b,1], Qinhua Chen [b], Lina Tang [a], Junlin Liu [a], Yujie Sun [a], Qiming Liu [c], Yulin Zhang [a,d,**], Guo-jun Zhang [a,d,***], Shaowei Chen [c,*]

[a] School of Laboratory Medicine, Hubei University of Chinese Medicine, Wuhan 430065, China
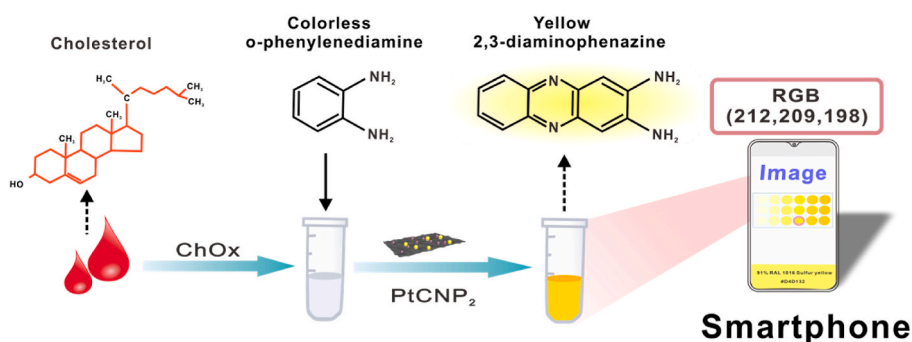[b] Shenzhen Baoan Authentic TCM Therapy Hospital, Shenzhen, 518101, China
[c] Department of Chemistry and Biochemistry, University of California, Santa Cruz, CA 95060, USA
[d] Hubei Shizhen Laboratory, Wuhan, Hubei 430065, China

HIGHLIGHTS

- *P*-doped carbon nitride (CNP$_2$) prepared by thermal annealing of urea and NH$_4$PF$_6$.
- PtCNP$_2$ obtained by atomic dispersion of Pt into CNP$_2$ by thermal refluxing.
- PtCNP$_2$ exhibits peroxidase-like activity under physiological pH.
- Smartphone-assisted visual sensing of cholesterol with PtCNP$_2$ and cholesterol oxidase.
- Demonstration of rapid detection of cholesterol in serum and food.

GRAPHICAL ABSTRACT

ARTICLE INFO

ABSTRACT

Cholesterol is an important lipid compound found in a variety of foods, and its level in human blood is closely related to human health. Therefore, development of rapid and accurate POCT (point-of-care testing) methods for cholesterol detection is crucial for assessing food quality and early diagnosis of diseases, in particular, in a resource-limited environment. In this study, a smartphone-assisted colorimetric biosensor is constructed based on platinum,phosphorus-codoped carbon nitride (PtCNP$_2$) for the rapid detection of cholesterol. Phosphorus-doped carbon nitride is prepared by thermal annealing of urea and NH$_4$PF$_6$, into which platinum is atomically dispersed by thermal refluxing. The obtained PtCNP$_2$ exhibits an excellent peroxidase-like activity under physiological pH, whereby colorless *o*-phenylenediamine (OPD) is oxidized to colored 2,3-diaminophenazine (DAP) in the presence of hydrogen peroxide (H$_2$O$_2$), which can be produced during the oxidation of cholesterol by cholesterol oxidase. A smartphone-assisted visual sensing system is then constructed based on the color recognition software, and rapid on-site detection of cholesterol is achieved by reading the RGB values. Meanwhile, the

generated DAP shows an apparent fluorescence signal and can realize highly sensitive detection of cholesterol by the change of the fluorescence signal intensity. Such a cholesterol sensor exhibits a wide linear detection range of 0.5–600 μg mL^{-1} and a low detection limit of 59 ng mL^{-1}. The practicality of the sensor is successfully demonstrated in the rapid detection of cholesterol in serum and food.

1. Introduction

Cholesterol is a key part of cell membranes and an essential nutrient, playing a crucial role in maintaining the structural integrity of cells and the normal functions of the nervous, endocrine, and reproductive systems, as well as the synthesis of bile acids [1]. However, chronically high serum cholesterol can lead to serious health disorders, such as cardiovascular disease and obesity [2,3]. One of the most effective strategies to control cholesterol levels in humans is to reduce the intake of foods with a high cholesterol content [4,5]. Therefore, development of simple POCT (point-of-care testing) methods for the detection of cholesterol in food and blood is essential for the assessment of food quality and early diagnosis of diseases associated with high cholesterol, in particular, in a resource-limited environment, as well as for providing therapeutic recommendations and evaluation of drug efficacy [6].

Currently, immunoassay [7], electrochemistry [8], high-performance liquid chromatography (HPLC) [9], and enzymatic approaches [10] have been used for cholesterol detection; yet these technologies typically entail complicated sample handling, drawn-out analytical processes, and sophisticated instrumentation, which restrict their widespread uses. Such issues can be mitigated by using visualization approaches where target detection is realized by direct observation of the color change with naked eyes. Indeed, sch a strategy has been widely employed in the detection platforms of various sensors [11,12]. For instance, horseradish peroxidase (HRP) catalyzes the oxidation of colorless substrates, such as 3,3,5,5-tetramethylbenzidine (TMB) and *o*-phenylenediamine (OPD), to colored products, in the presence of hydrogen peroxide (H$_2$O$_2$) [13]. In conjunction with cholesterol oxidase (ChOx) which can catalyze the oxidation of cholesterol and produce H$_2$O$_2$, HRP-based sensors have been developed for the visual detection of cholesterol. However, the practical applications of HRP-based sensors are limited because of the instability, low catalytic activity, and vulnerability of HRP to environmental and other conditions. Nanoenzymes have recently emerged as effective alternatives to natural enzymes, due to their competitive catalytic activity and excellent structural stability [14]. For instance, Li et al. [15] prepared a nanocomposite (NSC/Co$_{1-x}$S) with Co–S compounds loaded onto *N,S*-codoped carbon for the detection of human serum total cholesterol, and observed the best catalytic activity under acidic conditions (pH = 3.6). This deviated markedly from the physiological condition (pH = 7.6) which is needed for the optimal performance of ChOx. Such poor compatibility of nanoenzymes and ChOx compromised the overall catalytic efficiency of the sensor and accuracy of the results [16,17]. Within this context, it is of critical importance to prepare nanoenzymes that exhibit a high catalytic activity under physiological conditions.

Single-atom catalysts (SACs) have emerged as attractive options [18–22], where the homogenous active sites and high atom utilization efficiency lead to markedly enhanced activity and selectivity as compared to the traditional nanoparticle counterparts [23]. Among these, Pt SACs represent a uniquely promising candidate. For instance, Chen et al. [24] directly converted platinum nanoparticles (Pt NPs) into single atoms by reversing the thermal sintering process, which fully exposed the metal catalytic sites and resulted in tunable atomic structure and electronic properties, thus significantly improving the enzyme-like activity and selectivity. Experimentally, carbon nanotubes [25], graphene [26], and graphitic carbon nitride (g-C$_3$N$_4$) [27] have been used extensively as the supporting substrates, where the metal-support interactions and the electron transfer between the metal atoms and coordinating moieties of the supporting scaffold can exert a significant

impact on the catalytic activity of SACs [28]. For instance, Ou et al. [29] loaded Pt SACs on g-C$_3$N$_4$ nanosheets using a two-step procedure, and observed an improved performance in the photocatalytic evolution of H$_2$ and photooxidation of NO. Similarly, Zhu's group placed Pt single atoms onto g-C$_3$N$_4$, and the effective dispersion of the Pt atomic active sites led to an increase of the charge separation efficiency and hence photocatalytic performance towards hydrogen production [30]. Nevertheless, the application of g-C$_3$N$_4$ supported Pt SACs for electrochemical analysis is generally limited due to the poor electrical conductivity of g-C$_3$N$_4$. This can be mitigated by doping of select heteroatoms [31], such as oxygen (O) [32], boron (B) [33], sulfur (S) [34], and phosphorus (P) [35]. Among these, P doping has been demonstrated to improve the electrical conductivity of g-C$_3$N$_4$ by altering the energy band structure and electron distribution, promoting charge transfer, and hence increasing the catalytic activity and selectivity of the nanocomposite [36]. Meanwhile, P doping can enhance the catalytic activity by altering the electronic configuration and coordination environment of the central metal atoms. For example, Ding et al. [37] introduced phosphorus heteroatoms to SACs, and observed a significantly increased peroxidase-like activity and selectivity.

In this study, we constructed a fast and convenient multi-mode platform for cholesterol detection based on the combination of ChOx and P-doped g-C$_3$N$_4$ embedded with platinum single atoms. The P-doped g-C$_3$N$_4$ was first prepared by thermal annealing of urea and NH$_4$PF$_6$, and Pt was atomically dispersed into the structural scaffold by a thermal refluxing method. The resulting PtCNP$_2$ nanocomposites exhibited a good peroxidase-like activity under physiological conditions in the oxidation of colorless OPD to colored 2,3-diaminophenazine (DAP). In conjunction with ChOx, a smartphone-based sensing platform was constructed for the visual detection of cholesterol, where digital images were taken of the cholesterol reaction system at different concentrations, and the RGB values were analyzed through the color recognition app "Color Picker", leading to rapid and accurate detection of cholesterol. Meanwhile, the unique fluorescence emission of DAP was exploited for sensitive and specific detection of cholesterol. Such a multi-mode detection allowed the sensing platform for the analysis of actual clinical samples, demonstrating high potential for practical applications.

2. Experimental section

2.1. Chemicals

Cholesterol and ChOx were purchased from Aladdin Ltd (Shanghai, China). Hexane, anhydrous ethanol, OPD, hydrogen peroxide (H$_2$O$_2$, 30%, w/w), potassium hydroxide (KOH), calcium chloride (CaCl$_2$), magnesium chloride (MgCl$_2$), potassium chloride (KCl), sodium chloride (NaCl), glucose, sucrose, glycine, L-lysine, and urea were purchased from Sinopharm Chemical Reagents Co. Ltd. (Shanghai, China). Ammonium hexafluorophosphate (NH$_4$PF$_6$) and potassium trichloro (ethylene) platinate (II) hydrate (Zeise's salt, KPtCl$_3$(C$_2$H$_4$)) were purchased from Sigma-Aldrich. Ultrapure water was provided by a Millipore water purification system (18.2 MΩ cm, Milli-Q Direct8).

2.2. Synthesis of PtCNP$_2$ nanocomposites

PtCNP$_2$ nanoenzymes were prepared by following a procedure reported previously [38]. As shown in Scheme 1, in the first step to prepare P-doped g-C$_3$N$_4$, urea (10 g) was mixed with NH$_4$PF$_6$ (1 g) in a crucible,

which was covered and heated in air at a rate of 2 °C min^{-1} to 300 °C and kept at 300 °C for 3 h. The resulting white solid was ground into powders and heated again in air at a rate of 2 °C min^{-1} to 520 °C and kept at this temperature for 4 h. The resulting yellow solid was collected, washed with nanopure water, and dried overnight in a vacuum oven to obtain P-doped g-C$_3$N$_4$ (denoted as CNP$_2$).

The CNP$_2$ produced above (50 mg) was dispersed into an acetone and isopropanol solution (4 and 1 mL, respectively) under sonication for an hour. Zeise's salt (50 mg) was dissolved in acetone (5 mL) in a separate vial under magnetic stirring in an ice bath, into which was added KOH (20 mg) in a small amount of water under stirring for 40 min, and the KCl salt precipitate could be seen to accumulate on the wall of the glass vial. The carbon nitride dispersion was immersed in an ice bath under vigorous stirring for 10 min, into which was then added the Zeise's salt solution under magnetic stirring for 40 min, before the solution was subject to centrifugation at 6000 rpm for 10 min. The precipitate was collected and washed five times with acetone to remove unreacted platinum salts and contaminants. The material was dried overnight in a vacuum drying oven to obtain PtCNP$_2$.

2.3. Structural characterization

The surface morphology and structure of PtCNP$_2$ were characterized using transmission electron microscopy (TEM) and high angle annular dark field-scanning transmission electron microscopy (HAADF-STEM). X-ray photoelectron spectroscopy (XPS) studies were conducted to analyze the elemental composition and valency of the nanocomposites. Fluorescence measurements were conducted with a Hitachi-4600 fluorescence spectrophotometer. HPLC-MS tests were conducted with an AB SCIEX 6500+ mass spectrometer and an LC-40D Shimadzu liquid chromatographer. The chromatographic conditions included a column of ZORBAX Eclipse XDB- (4.6 × 250 mm, 5 μm), mobile phase of 0.1% formic acid aqueous solution:acetonitrile (50:50), isocratic elution, analysis time of 5 min, flow rate of 0.5 mL min^{-1}, column temperature 40 °C, injection volume of 3 μL. The MS analysis was performed by using the electrospray ionization source (ESI) in the positive ion mode and multiple reaction monitoring (MRM) for ion detection, spray voltage 5500 V, curtain gas (CUR) of 35 psi, medium collision gas (CAD), ion source temperature (TEM) of 550 °C and ion source gas stream 2 (GS2) at 55 psi.

2.4. Determination and kinetic analysis of peroxidase activity of PtCNP$_2$ nanoenzymes

OPD was employed in this experiment as a chromogenic substrate for the oxidation reaction to assess the peroxidase-like activity of PtCNP$_2$. 10 μg mL^{-1} PtCNP$_2$, 30 μM H$_2$O$_2$, and 30 μg mL^{-1} OPD were mixed, and a phosphate buffered saline (PBS, pH = 7.4) was added to make the final volume of the reaction system at 1 mL. The reaction was carried out for 30 min at room temperature (25 °C), and the fluorescence emission spectra were collected from 510 to 650 nm at the excitation wavelength of 414 nm.

In the analysis of the peroxidase-like activity of PtCNP$_2$, steady-state kinetic experiments were carried out at 25 °C using 10 μg mL^{-1} PtCNP$_2$ as the catalyst. For kinetic analysis using H$_2$O$_2$ as the substrate, 30 μg mL^{-1} OPD and different concentrations of H$_2$O$_2$ (0.5, 1, 2, 3, 4, and 5 mM) were added. Conversely, for kinetic analysis using OPD as the substrate, the peroxidase-like activity was tested by adding 30 μM H$_2$O$_2$ and different concentrations of OPD (0, 0.1, 0.2, 0.4, 0.6, 0.8, and 1 mM) for a reaction time of 10 min. 200 μL of the reaction solution was
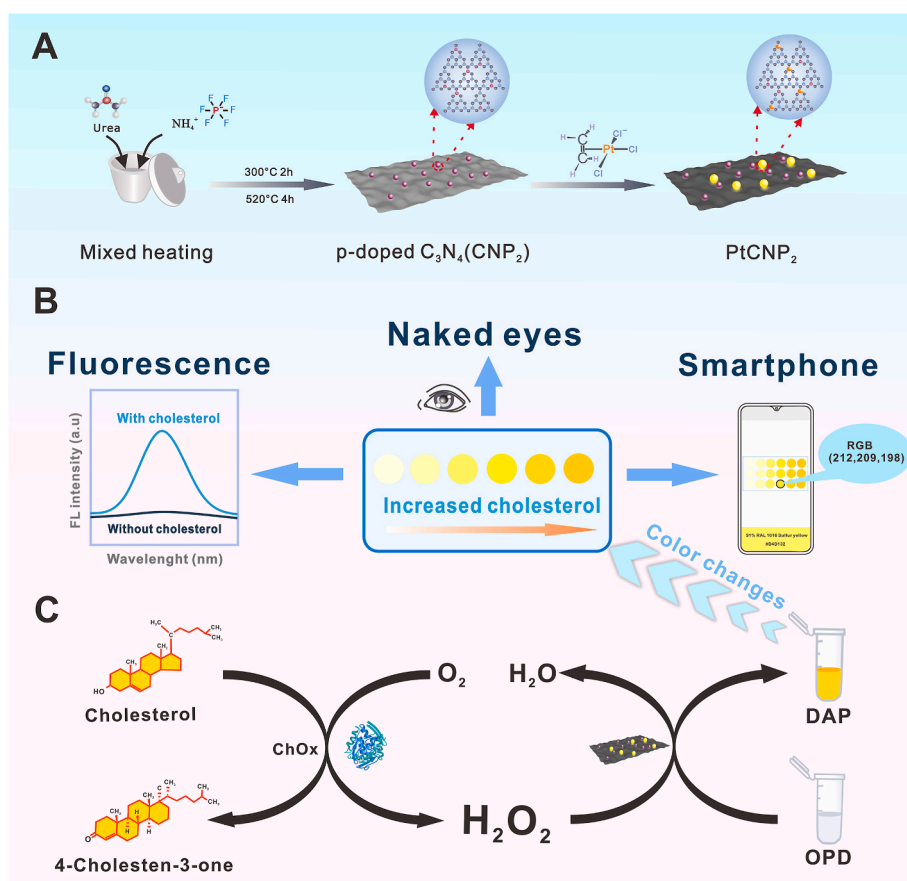
Scheme 1. Schematic representation of visual detection of cholesterol based on PtCNP$_2$ nanoenzymes. (a) Synthesis of PtCNP$_2$ nanocomposites. (b) Graphic illustration of smartphone-based colorimetric detection of cholesterol, where ChOx and PtCNP$_2$ work concertedly, as depicted in panel (c).

pipetted into a 96-well plate, and the absorbance values were determined by an enzyme marker at 420 nm. The kinetic parameters were calculated according to the Michaelis-Menten equation (equation (1)),

$$1/v = K_m/v_{max}[S] + 1/v_{max} \tag{1}$$

where K_m is the Michaelis-Menten constant, v_{max} is the maximum rate of the enzymatic reaction, [S] is the substrate concentration, and v is the initial reaction rate, which can be calculated from $A/(b\varepsilon_{OPD}t)$, with A being the solution absorbance, b the path length of light, ε_{OPD} the OPD molar absorption coefficient, and t the reaction time. The lower the K_m value, the higher affinity of the enzyme to the substrate.

2.5. PtCNP$_2$ sensing platform for cholesterol detection

In the detection of cholesterol, 100 µg mL^{-1} of ChOx and different concentrations of cholesterol (final concentrations 0.5, 10, 100, 200, 400, 600, and 800 µg mL^{-1}) were added to 50 µL of a PBS buffer (pH = 7.4) and incubated at 37 °C for 30 min before passing through a 0.45 mm cellulose mixture filter. Then PtCNP$_2$ and OPD were added to the filtrate, and the solution volume was increased to 1 mL by the addition of a PBS buffer solution (pH = 7.4). The solution was further incubated at 25 °C for 30 min, and the fluorescence emission spectra were collected at 414 nm excitation. The measurements were repeated three times for each experimental condition to calculate the standard deviation (n = 3).

2.6. Cholesterol detection in serum and food samples

In the cholesterol assay in human serum, in order to prevent other substances within the serum from interfering with the experiment, the serum samples were subject to a pretreatment. Experimentally, 0.5 mL of human serum was mixed with 3.5 mL of ethanol and 4.0 mL of deionized water, followed by 2.0 mL of hexane. The mixture was under shaking for 2 min, and stood for a few minutes when the upper hexane portion was removed. The extraction was repeated twice, before the solution was dried with a nitrogen stream. The remaining solids were collected and dissolved in 0.5 mL of a mixture of ethanol and PBS (1:4). At 37 °C, 100 µL of the test solution and ChOx solution (100 µg mL^{-1}) were added to 50 µL of a PBS buffer (pH = 7.4) (section 2.5). The results obtained were methodologically compared with the hospital test results and the results obtained by high-performance liquid chromatography-mass spectrometry (HPLC-MS) measurements.

To test the cholesterol content in eggs, the egg white was removed and 1 g of the egg yolk was collected and added into 10 mL of a 50% KOH solution and 30 mL of anhydrous ethanol under shaking. The solution was subject to ultrasonic saponification for 30 min in a water bath at a constant temperature of 75 °C [39]. When the solution was cooled down to room temperature, 10 mL of a 25% NaCl solution and 10 mL of hexane were added under shaking for 1 min, and the solution was let to stand for 5 min, when the upper layer of the hexane phase was collected. The extraction was repeated twice and the collected hexane solution was washed with deionized water several times and dried with a nitrogen stream, before being dispersed into 1 mL of anhydrous ethanol to dissolve the cholesterol. The solution was filtered through a 0.45 µm filter before spectroscopic measurements.

In the cholesterol analysis of milk, 5 mL of pure milk (commercially available), 10 mL of a 50% KOH solution and 30 mL of anhydrous ethanol were thoroughly mixed under saponification in a water bath at a constant temperature of 100 °C for 1 h [40]. When the solution was cooled down to room temperature under running water, the same extraction, concentration and analysis procedure was employed as that described above for egg yolks.

2.7. Smartphone-assisted colorimetric detection of cholesterol

Different concentrations of cholesterol, ChOx, PtCNP$_2$, OPD, and PBS

buffer solution were mixed according to the process described in section 2.5. 200 µL of the mixed solution was added to a clean 96-well plate, where a digital image was captured using a smartphone (Mi 9 SE, Xiaomi Technology Co., Ltd., China), and imported into the color recognition app "Color Picker'. The area was selected by dragging and dropping, and the color parameters (RGB values) of the selected area were obtained for analysis.

3. Results and discussion

3.1. Morphological and structural characterization of PtCNP$_2$

The structure of PtCNP$_2$ was first examined by TEM measurements. From Fig. 1a, PtCNP$_2$ can be seen to possess a porous, lamellar structure (lateral size of a few hundred nm) without apparent particulates, consistent with the typical morphology of g-C$_3$N$_4$ [41,42]. In HAADF-STEM measurements (Fig. 1b), one can see that a number of bright spots, which were most likely individual Pt atoms, were embedded within the g-C$_3$N$_4$ scaffold. In the corresponding elemental mapping analysis based on energy-dispersive X-ray spectroscopy (EDS) (Fig. 1c), the elements of C, N, P, Pt, and O can be readily identified and exhibit a homogeneous distribution across the sample, consistent with the formation of PtCNP$_2$ that consisted of P-doped C$_3$N$_4$ loaded with Pt single atoms [38].

XPS experiments were then carried out to evaluate the elemental composition and valency of PtCNP$_2$. From the survey spectrum in Fig. 2a, Pt 4f (74 eV), P 2p (133 eV), Cl 2p (285 eV), C 1s (285 eV), N 1s (399 eV), and O 1s (532 eV) can be readily resolved in PtCNP$_2$, with an elemental content of 2.03 at% for Pt, 0.69 at% for P, 0.75 at% for Cl, 52.25 at% for C, 21.45 at% for N, and 22.83 at% for O (Table S1). Fig. 2b shows the high-resolution scan of the C 1s electrons where three peaks were deconvoluted at 284.80, 286.59, and 288.04 eV, due to the aromatic ring's sp^2 C, C–N≡C, and C–P, respectively [43]. The N 1s spectrum is shown in Fig. 2c, which entails two peaks at 398.63 eV and 400.53 eV that can be ascribed to the sp^3 hybridized graphitic nitrogen N-(C)$_3$ and sp^2 hybridized pyridine nitrogen (C–N≡C), respectively [44]. The high-resolution scan of the Pt 4f electrons is displayed in Fig. 2d, which consisted of two $4f_{7/2}/4f_{5/2}$ doublets, Pt(II) at 72.54/75.85 eV and Pt(IV) at 74.17/77.51 eV (Table S2) [43,45]. The P 2p spectrum was depicted in Fig. S1a, where the P $2p_{3/2}$ binding energy of 133.41 eV (Table S2) is consistent with that of the P–C bond reported in the literature, suggesting successful doping of P into the g-C$_3$N$_4$ skeletons [46]. The high-resolution scan of the Cl 2p electrons is shown in Fig. S1b, where the binding energy of 197.86/199.36 eV is consistent with that previously reported for PtCl-containing complexes (Table S2) [47]. In fact, the atomic ratio of Cl to Pt in PtCNP$_2$ was calculated to be 0.37:1, suggesting partial retention of the original Cl ligands in the Zeise's salt precursor (Cl:Pt ratio 3:1) when Pt was embedded into g-C$_3$N$_4$.

3.2. Peroxidase-like activity assessment and kinetic analysis of PtCNP$_2$ nanoenzymes

Using a standard OPD-H$_2$O$_2$ colorimetric system, the peroxidase-like activity of PtCNP$_2$ was then assessed (Fig. 3a). Note that a PBS solution containing only H$_2$O$_2$, OPD, or OPD + H$_2$O$_2$ was colorless with no fluorescence emission (Fig. S2 and inset). From Fig. 3b and inset, one can see that the mixed solution of PtCNP$_2$+H$_2$O$_2$ was also colorless and non-fluorescent, whereas a faint yellow color emerged with PtCNP$_2$+OPD, along with a weak fluorescence emission peak at 570 nm; and the yellow color became markedly more intense with PtCNP$_2$+OPD+H$_2$O$_2$, and the fluorescence emission intensity increased by more than four folds. This is because PtCNP$_2$ catalyzed the formation of hydroxyl radicals (•OH) from H$_2$O$_2$ (which was confirmed by electron spin resonance measurements, Fig. S3), and •OH subsequently catalyzed the transformation of colorless OPD into yellow DAP, which showed a
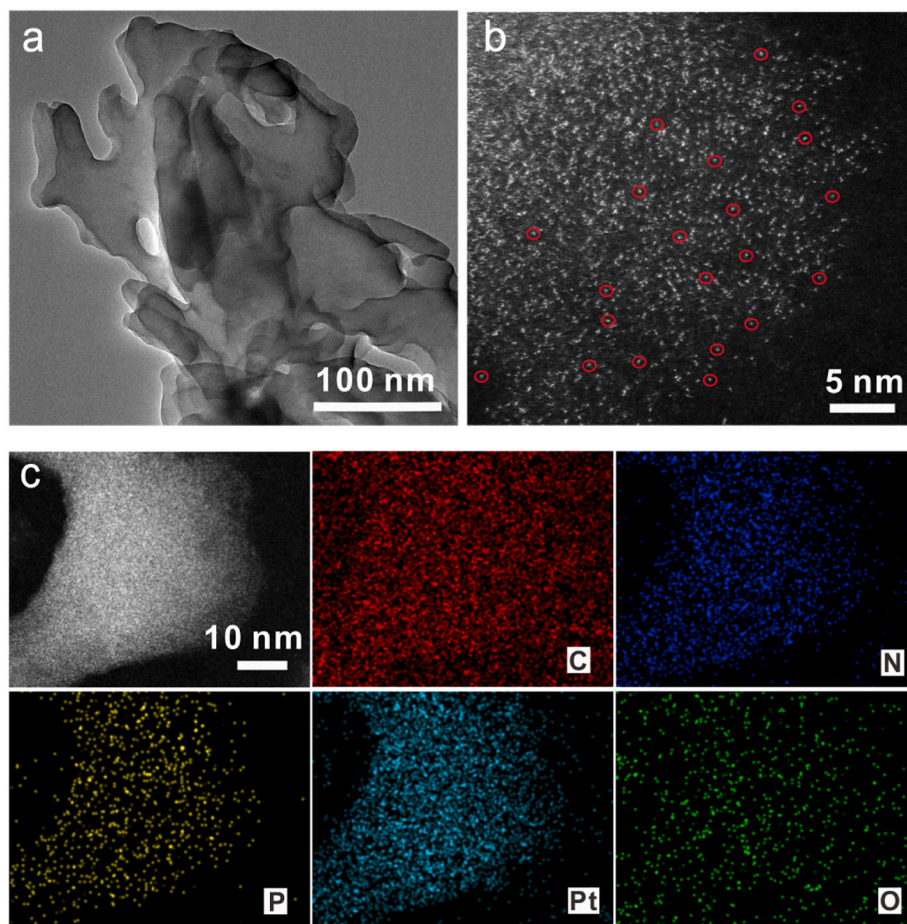
Fig. 1. (a) TEM and (b) HAADF-STEM images of PtCNP$_2$. (c) HAADF image and the elemental maps of C, N, P, Pt, and O.

prominent emission peak at 570 nm [13]. Notably, there was no change in the hue of the solution and no conspicuous emission peaks were seen with mixed solutions of Pt-free CNP$_2$+H$_2$O$_2$, CNP$_2$+OPD, or CNP$_2$+H$_2$O$_2$+OPD (Fig. 3c and inset). These results showed that PtCNP$_2$ indeed possessed peroxidase-like activity and could act as a nanoenzyme.

Colorimetric experiments were then used to investigate the peroxidase-like catalytic activity of PtCNP$_2$ in the oxidation of OPD. As shown in Fig. S4, in the simultaneous presence of PtCNP$_2$ and H$_2$O$_2$, OPD was oxidized and the solution produced a strong absorption peak (λ_{max}) at 420 nm, indicative of the high catalytic activity of PtCNP$_2$. To further investigate the steady-state kinetics of PtCNP$_2$, typical Michaelis-Menten curves were obtained by varying the concentrations of the substrates (OPD and H$_2$O$_2$) (Fig. 3d and f). The corresponding Lineweaver-Burk curves showed good linearity (Fig. 3e and j). The calculated Michaelis-Menten constants (K_m) are shown in Table S3. When OPD was used as the substrate, the K_m value of PtCNP$_2$ was 0.061 mM, which was almost one order of magnitude lower than that of natural HRP (0.59 mM), indicating that the affinity of PtCNP$_2$ to OPD was stronger than that of HRP, likely because of the large specific surface area and abundant binding sites of PtCNP$_2$. When H$_2$O$_2$ was used as the substrate, the K_m value of PtCNP$_2$ was 0.356 mM, which was very close to that for HRP (0.34 mM), suggesting comparable affinity to H$_2$O$_2$. In fact, the K_m values of PtCNP$_2$ for OPD and H$_2$O$_2$ are lower than most peroxidase nanoenzymes reported in the literature, suggesting good peroxidase-like activity of PtCNP$_2$ (Table S3).

We also examined the stability of PtCNP$_2$ by repeating the tests for 7 consecutive days, and the results are shown in Fig. S5, where the catalytic activity remained virtually unchanged, confirming excellent stability of the PtCNP$_2$ nanoenzyme.

3.3. Parameter optimization

The catalytic activity of PtCNP$_2$ can be used to accomplish quick and visual detection of cholesterol in conjunction with ChOx that catalyzes the production of H$_2$O$_2$ from cholesterol oxidation. OPD serves as a chromogenic substrate, and H$_2$O$_2$ serves as a signal agent. Before applying it to the measurement of cholesterol, we first checked the H$_2$O$_2$ test based on PtCNP$_2$. The activity of nanoenzymes is known to be closely related to the experimental conditions. In this investigation, the concentration of OPD and PtCNP$_2$, reaction time, temperature, and pH were identified as the major experimental variables for the optimization of H$_2$O$_2$ detection. First, we investigated the impact of OPD and PtCNP$_2$ concentrations and used the fluorescence transfer efficiency ((F–F$_0$)/F$_0$, where F and F$_0$ are fluorescence emission intensities in the presence and absence of H$_2$O$_2$, respectively) as a criterion for the ideal conditions. As shown in Fig. 4a and b, (F–F$_0$)/F$_0$ reached the highest value at the OPD concentration of 30 μg mL^{-1} and PtCNP$_2$ of 10 μg mL^{-1}. These optimal concentrations were then chosen in the subsequent studies in order to prevent the inappropriate selection of enzyme and substrate dosage, which could have detrimental effects on the experiments such as nonspecific reaction, enzyme inhibition, and competition of substrate.

Second, we optimized the reaction temperature. The enzyme can only remain active within a certain temperature range. Beyond this range, the enzyme may become denatured or potentially lose its catalytic activity. From Fig. S6a, it can be seen that 25 °C was the ideal reaction temperature. We then investigated the ideal response time for the PtCNP$_2$ sensing device within the range of 5–40 min. An incomplete reaction and inadequate substrate conversion may occur if a reaction time is too short, whereas overreaction and experimental oversaturation may result from too long a reaction time. Therefore, selecting the right
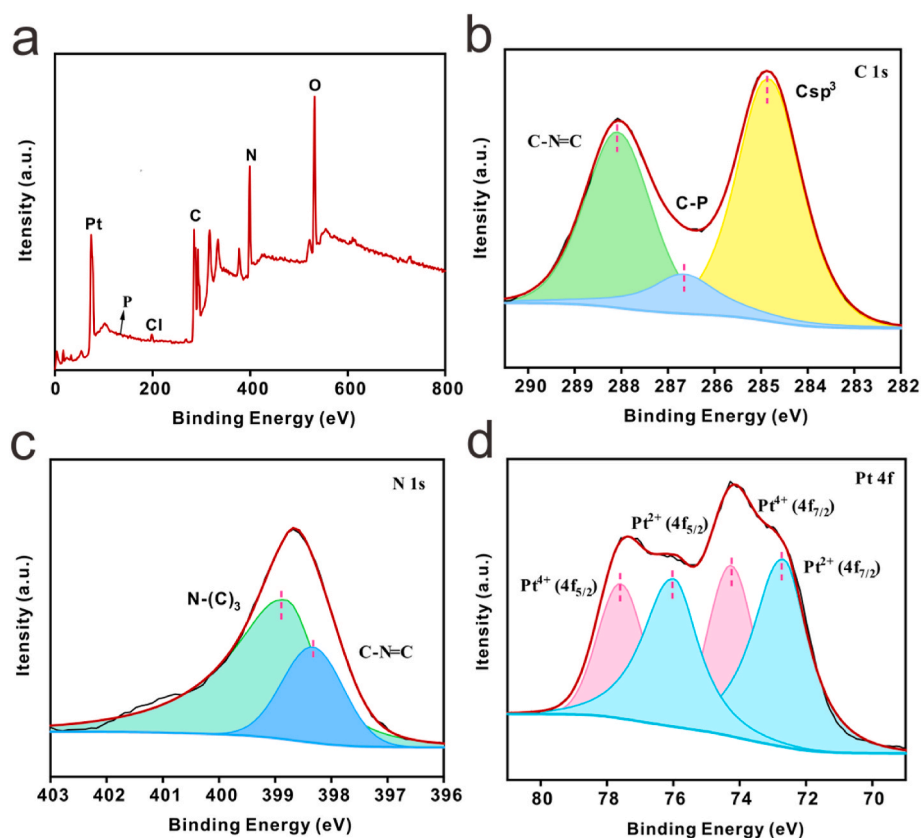
Fig. 2. (a) XPS survey spectrum of PtCNP$_2$ and corresponding high-resolution scans of the (b) C 1s, (c) N 1s and (d) Pt 4f electrons.

reaction time is essential for attaining effective catalysis. From Fig. S6b, it can be seen that the (F–F$_0$)/F$_0$ value peaked at about 30 min, indicating that 30 min was the ideal reaction time.

Finally, we evaluated the effect of pH (Fig. S7), where the fluorescence emission can be seen to peak within the pH range of 6.5 (weakly acidic) to 7.4 (physiological condition). Yet as the fluorescence emission of the blank control was also high under the weak acid condition (pH 6.5), the (F–F$_0$)/F$_0$ value actually reached the maximum at pH = 7.4, suggesting high catalytic activity and low background interference of the PtCNP$_2$ nanoenzyme under physiological conditions. Therefore, subsequent tests were carried out under the ideal conditions outlined above in order to maximize the efficacy and efficiency of the sensing platform.

3.4. Cholesterol testing

We first examined the solution color changes and fluorescence response for H$_2$O$_2$ levels in the range of 2~2000 µM under the ideal experimental conditions identified above. As seen in Fig. S8a, as the concentration of H$_2$O$_2$ increased from 0 to 2000 µM, the fluorescence emission of DAP at 570 nm steadily rose (Fig. S8b), and the color of the reaction solution gradually changed from light yellow to dark yellow (Fig. S8c and inset). Notably, the fluorescence emission intensity exhibited an excellent linear relationship with the H$_2$O$_2$ concentration in the range of 2–70 µM (F = 10.9649 [H$_2$O$_2$] + 306.8404, where R^2 = 0.9982), and the limit of detection (LOD) (3σ k^{-1}, where k is the slope of the curve, and σ is the standard deviation) was as low as 224 ng mL^{-1}.

Cholesterol was then analyzed by observing the change in color of the solution (from colorless to yellow) and the output of the fluorescence signal. Cholesterol oxidation is catalyzed by ChOx to produce cholest-4-en-3-one and H$_2$O$_2$, and H$_2$O$_2$ then reacts quickly with OPD catalyzed by PtCNP$_2$. The experimental results are displayed in Fig. 4c and d. One can see that 0.1 mg mL^{-1} of ChOx was the ideal concentration, and 30 min

was the ideal response time. Additionally, we studied the impact of pH on cholesterol detection (Fig. S9). The results were in line with the H$_2$O$_2$ assay, with a maximum (F–F$_0$)/F$_0$ at pH 7.4, confirming that the PtCNP$_2$ nanoenzyme possessed the high catalytic activity for cholesterol detection under physiological settings, which could be exploited for cholesterol assay. Fig. 5a shows that the fluorescence emission intensity of DAP varies with cholesterol concentration (0–800 µg mL^{-1}), and the results at 0.5 µg mL^{-1} of cholesterol were also recognizable by naked eyes (Fig. 5b). When the cholesterol concentration was between 0.5 and 600 µg mL^{-1}, the fluorescence emission intensity increased linearly with the cholesterol concentration, F = 0.4517 [cholesterol] + 121.8489 (R^2 = 0.9914), with a LOD of about 59 ng mL^{-1}. Notably, one can see that such a performance of cholesterol detection is highly comparable to those with other leading methods reported in the literature (Table S4).

Studies were also carried out to investigate the selectivity of the visual fluorescence sensing platform based on PtCNP$_2$ for H$_2$O$_2$ and cholesterol. As seen in Fig. S8d, H$_2$O$_2$ was the only agent that caused the assay solution to change color and the fluorescence signals to be amplified even at high concentrations of interfering substances, such as sugars, amino acids, and common inorganic ions, all at a concentration of 100 µM. As shown in Fig. 5c, the interfering substances sucrose, glucose, urea, uric acid, MgCl$_2$, L-lysine, and others (all at 4 mg mL^{-1}) had almost no effect on the sensing platform. Only in the presence of the target cholesterol did the color of the solution change to yellow and the fluorescence emission intensity at 570 nm increase significantly. It shows that the present biosensor possessed superb selectivity for cholesterol detection, which could be ascribed to ChOx's matrix-specific catalytic action. In conclusion, the PtCNP$_2$-based sensing system demonstrated good sensitivity, acceptable selectivity for H$_2$O$_2$ and cholesterol detection.
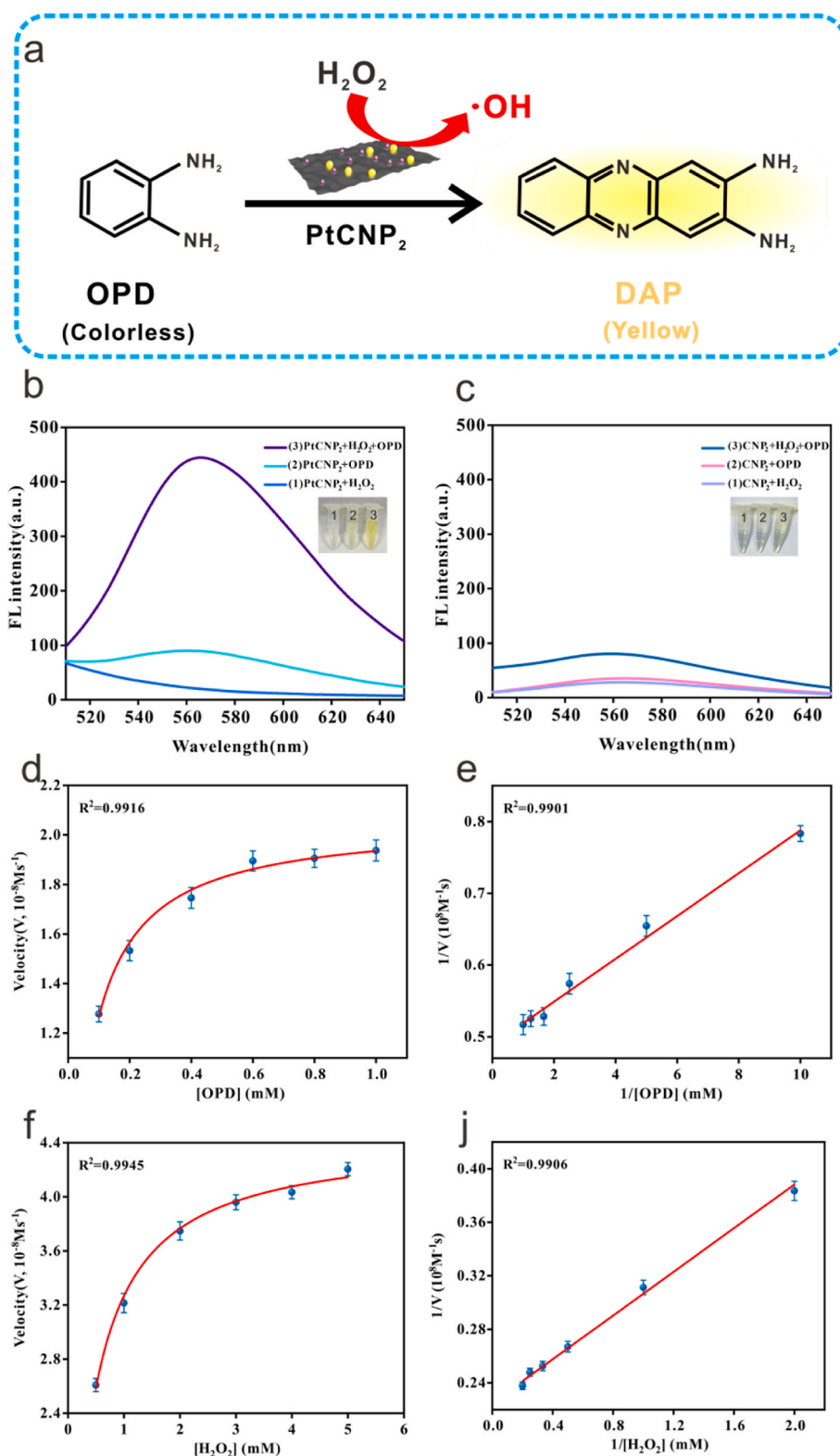
Fig. 3. (a) Schematic illustration of PtCNP$_2$ catalyzed H$_2$O$_2$ oxidation of OPD. (b) Fluorescence spectra of different reaction systems, (1) PtCNP$_2$+H$_2$O$_2$, (2) PtCNP$_2$+OPD, (3) PtCNP$_2$+H$_2$O$_2$+OPD under 414 nm excitation. The concentration of OPD is 30 μg mL^{-1}, H$_2$O$_2$ is 30 μM, and PtCNP$_2$ is 10 μg mL^{-1} in PBS at pH 7.4. (c) Fluorescence spectra of CNP$_2$+H$_2$O$_2$, CNP$_2$+OPD, and CNP$_2$+H$_2$O$_2$+OPD under excitation of 414 nm. The concentrations of CNP$_2$, OPD, and H$_2$O$_2$ are 10 μg mL^{-1}, 30 μg mL^{-1} and 30 μM, respectively. The insets show the corresponding solution photographs. Michaelis–Menten plot of (d) OPD and (f) H$_2$O$_2$. Lineweaver–Burk plot of (e) OPD and (j) H$_2$O$_2$.
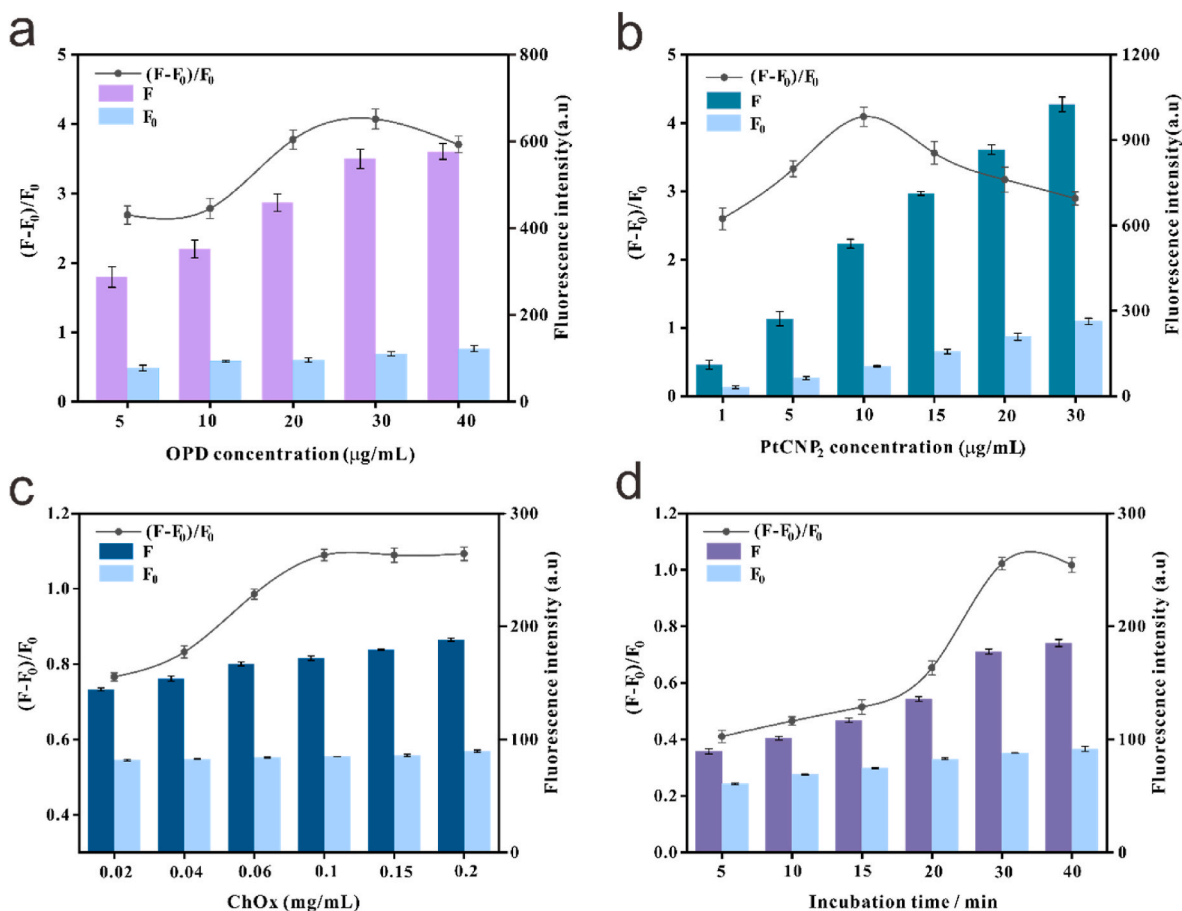
Fig. 4. Condition optimization for (a) OPD concentration, (b) PtCNP$_2$ concentration, (c) ChOx concentration, and (d) ChOx-catalyzed cholesterol reaction time.
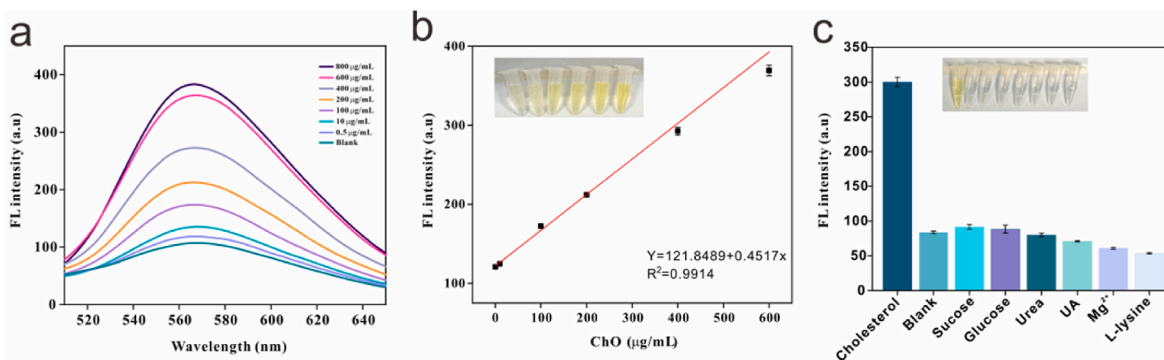

Fig. 5. (a) Fluorescence response profiles of the PtCNP$_2$-based fluorescent sensor for different concentrations of cholesterol. (b) Linear correlation between fluorescence response and cholesterol. (c) Selective examination of cholesterol detection with interfering substances of sucrose, glucose, urea, uric acid, MgCl$_2$, and L-lysine at 4 mg mL^{-1}, and a cholesterol concentration of 0.4 mg mL^{-1}. The inset shows the corresponding color change images. (For interpretation of the references to color in this figure legend, the reader is referred to the Web version of this article.)

3.5. Detection of cholesterol in real samples

Under simulated physiological settings, the PtCNP$_2$ nanoenzyme was then used to detect cholesterol in clinical serum, egg yolk, and pure milk samples, to confirm the practical application and accuracy of the results. Twenty serum samples were obtained from the Hubei Provincial Hospital of Traditional Chinese Medicine, and four samples each of pure milk and eggs were obtained from commercially available sources. These samples were then given the proper pretreatments (section 2.7) before being subjected to analysis and testing using the PtCNP$_2$-based platform, and the results were compared to traditional cholesterol assays

to assess the performance metrics of accuracy and stability (Table 1), where the results from the PtCNP$_2$ sensor were mostly in accord with those from the hospital method and the HPLC-MS tests, with a relative standard deviation (RSD) of 1.1–14.2% for PtCNP$_2$ and 1.8–7.4% for HPLC-MS. To assess the quantitative accuracy of the PtCNP$_2$ platform, the Pearson correlation analysis (Fig. S10) was also carried out between the detection findings of the PtCNP$_2$ sensor and those based on clinical methods and HPLC-MS. The findings demonstrated reasonable agreement between the results of the PtCNP$_2$ sensor and those of the hospital method and HPLC-MS (r = 0.9934 and r = 0.9899), and hence great sensitivity of PtCNP$_2$ for cholesterol detection in intricate biological

Table 1
Fluorescence determination of cholesterol content in human serum samples in comparison to results from the clinical data and HPLC-MS measurements.

Sample	Clinical Data (mg mL^{-1})	PtCNP$_2$ (mg mL^{-1})	RSD (%)	HPLC-MS (mg mL^{-1})	RSD (%)
normal serum 1	1.98	1.89 ± 0.13	6.9	2.04 ± 0.07	3.4
normal serum 2	1.62	1.66 ± 0.06	3.3	1.68 ± 0.12	7.2
normal serum 3	1.68	1.74 ± 0.06	3.6	1.65 ± 0.10	5.8
normal serum 4	1.87	1.90 ± 0.05	2.5	1.89 ± 0.11	5.6
normal serum 5	1.53	1.58 ± 0.04	2.7	1.60 ± 0.07	4.7
normal serum 6	1.45	1.52 ± 0.06	4.0	1.49 ± 0.05	3.1
normal serum 7	1.79	1.77 ± 0.06	3.3	1.80 ± 0.20	11.0
normal serum 8	1.50	1.54 ± 0.05	4.1	1.53 ± 0.09	5.6
normal serum 9	1.34	1.38 ± 0.03	2.0	1.35 ± 0.19	14.2
normal serum 10	1.76	1.81 ± 0.04	2.4	1.81 ± 0.06	3.2
obese serum 1	2.76	2.83 ± 0.08	2.8	2.78 ± 0.05	1.8
obese serum 2	2.62	2.67 ± 0.05	1.8	2.70 ± 0.03	1.1
obese serum 3	2.63	2.57 ± 0.10	3.8	2.65 ± 0.09	3.6
obese serum 4	2.40	2.53 ± 0.06	2.5	2.46 ± 0.05	2.0
obese serum 5	2.34	2.39 ± 0.11	4.8	2.37 ± 0.10	4.4
obese serum 6	2.39	2.31 ± 0.17	7.4	2.45 ± 0.09	3.8
obese serum 7	2.94	2.91 ± 0.10	3.6	3.12 ± 0.10	3.3
obese serum 8	2.88	2.95 ± 0.08	2.9	3.04 ± 0.06	1.9
obese serum 9	2.34	2.39 ± 0.10	4.4	2.35 ± 0.07	3.0
obese serum 10	2.37	2.48 ± 0.13	5.3	2.42 ± 0.03	1.3

samples.

Also, to further study the applicability of the PtCNP$_2$ sensor, the cholesterol levels in pure milk and egg yolks were also measured and compared to those of HPLC-MS. From Table S5, the RSD of the fluorescence results was 3.8%–6.9% with a Pearson correlation coefficient of 0.9909, suggesting good agreement between these two techniques (Fig. S11). Also, we conducted a recovery experiment using the conventional addition method to identify the presence of cholesterol in egg yolk1 and pure milk1 (Table S6). The spiking recoveries were in the range of 99.2%–104.1% with RSDs of 2.9%–4.6%. These findings showed that the PtCNP$_2$ biosensor possessed outstanding potential for practical clinical applications.

3.6. Smartphone-assisted colorimetric detection of cholesterol

To realize more convenient and accurate visual detection of cholesterol, a smartphone-assisted fluorescence sensing system was also constructed, as schematically depicted in Fig. 6a. The experimental conditions were the same as the fluorescence detection described above, and the images of the cholesterol reaction systems at different concentrations were recorded by using the photo function of a smartphone, and the color changes of the reaction systems were converted into the values of the red (R), green (G), and blue (B) channels by using the app "Color Picker". Fig. 6b shows the photographs of the reaction system in the presence of cholesterol at different concentrations (0–800 μg mL^{-1}), which exhibit a good linear relationship between (R + G)/B and

cholesterol concentration, (R + G)/B = 7.9311 [cholesterol] + 2.0956 (R^2 = 0.99652), with the LOD of 188 ng mL^{-1}. In addition, to investigate the applicability of the smartphone for cholesterol detection in complex environments, we detected cholesterol in the presence of several interfering substances. The results are shown in Fig. 6c, where the (R + G)/B values and reaction system colors in the presence of the interfering molecules or ions remained almost the same as those of the control. Only in the presence of cholesterol, did the (R + G)/B values and the color of the reaction system change significantly. Finally, we tested the cholesterol contents in various food products to verify the use of the method for real samples. The extracted test solutions (in eggs and pure milk) were mixed with ChOx, PtCNP$_2$, and OPD solutions (section 2.6), and digital photos were taken after a select period of reaction time, and the cholesterol contents of the test solutions were obtained by evaluating the (R + G)/B values (Table S5). The results were in general agreement with the fluorescence and HPLC-MS assays (Pearson correlation coefficients of 0.9987 and 0.9919, respectively; Table S7), with RSDs in the range of 2.7–6.4%. These results confirm that the smartphone-assisted colorimetric sensing system is a viable method for semi-quantitative detection and rapid on-site determination of cholesterol.

4. Conclusion

In this study, we prepared a nanoenzyme based on phosphorus-doped g-C$_3$N$_4$ embedded with platinum single atoms (PtCNP$_2$) and constructed a label-free, fast, and sensitive multimodal biosensor for instant cholesterol detection based on the excellent peroxidase-mimetic activity under physiological conditions. Compared with other existing biosensors for cholesterol detection, the PtCNP$_2$ sensing strategy showed more remarkable simplicity as it did not require specialized and expensive instrumentation or complicated operation steps. Meanwhile, the prepared PtCNP$_2$ nanoenzymes exhibited low background interference and high sensitivity in cholesterol detection, achieving ultra-sensitive detection of cholesterol in the linear range of 0.5–600 μg mL^{-1} with an LOD as low as 59 ng mL^{-1}. Meanwhile, PtCNP$_2$ also showed good applicability, selectivity, and accuracy and was successfully demonstrated to be suitable for cholesterol detection in clinical serum and food samples by naked-eye recognition and fluorescence signal readout, demonstrating high potential for the diagnosis and treatment of cholesterol-related diseases. Furthermore, a smartphone-assisted colorimetric sensing system based on the color recognition app was established and its ability to detect real samples was verified in food products, providing an advantageous tool for cholesterol detection in scenarios such as on-site and mobile environments.

Notably, one can envisage that the peroxidase-like activity of PtCNP$_2$ can be exploited for the sensing of other biological activities that also produce H$_2$O$_2$. This paves the way for the development of multi-indicator, multi-functional, and multi-modal biosensing. Relevant research is ongoing and results will be reported in due course.

CRediT authorship contribution statement

Meiling Chen: Writing – original draft, Investigation, Formal analysis, Data curation. **Yang Yang:** Resources, Investigation, Formal analysis, Data curation. **Qinhua Chen:** Formal analysis, Data curation. **Lina Tang:** Formal analysis, Data curation. **Junlin Liu:** Formal analysis, Data curation. **Yujie Sun:** Formal analysis, Data curation. **Qiming Liu:** Investigation, Formal analysis. **Yulin Zhang:** Writing – original draft, Supervision, Funding acquisition, Formal analysis, Data curation, Conceptualization. **Guo-jun Zhang:** Writing – original draft, Supervision, Funding acquisition, Formal analysis, Conceptualization. **Shaowei Chen:** Writing – review & editing, Supervision, Formal analysis, Conceptualization.
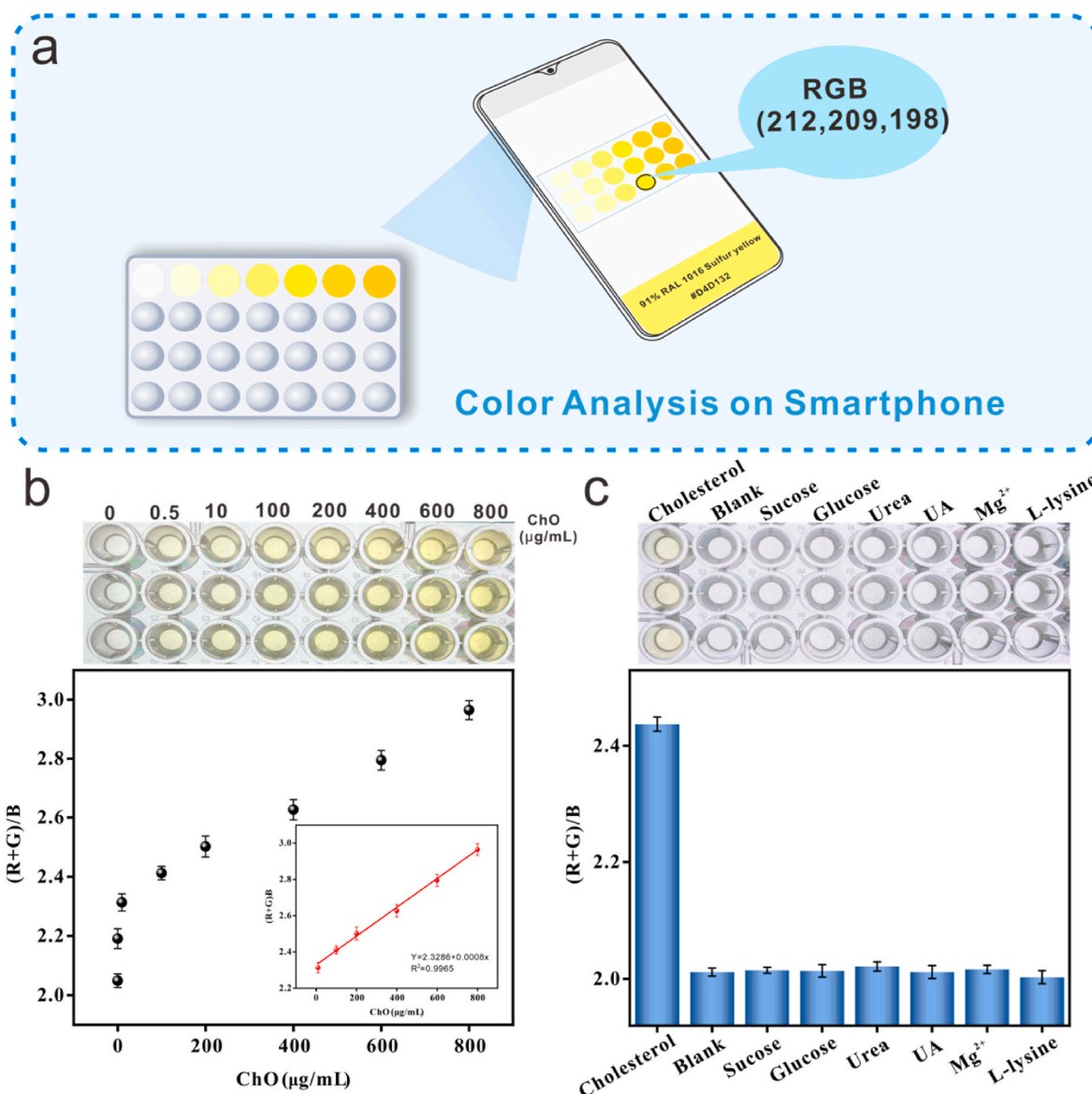
Fig. 6. (a) Schematic of the smartphone-assisted fluorescence sensing strategy for cholesterol visualization and detection. (b) Photographs of the reaction system in the presence of a different concentration of cholesterol (0–800 $\mu g\ mL^{-1}$), and the corresponding variation of $(R + G)/B$ with cholesterol concentration. (c) Selectivity of smartphone visualization detection is examined by the addition of various interferents at the cholesterol concentration of 0.1 mg mL^{-1} and interferent concentrations of 1 mg mL^{-1}. The corresponding solution photographs are shown on top of the graph and used for RGB analysis.

Declaration of competing interest

The authors declare that they have no known competing financial interests or personal relationships that could have appeared to influence the work reported in this paper.

Data availability

Data will be made available on request.

Appendix A. Supplementary data

Supplementary data to this article can be found online at https://doi.org/10.1016/j.aca.2024.342351.

References

[1] A. Wahlström, Sama I. Sayin, H.-U. Marschall, F. Bäckhed, Intestinal crosstalk between bile acids and microbiota and its impact on host metabolism, Cell Metabol. 24 (2016) 41–50.

[2] J. Cadet, K.J.A. Davies, Oxidative DNA damage & repair: an introduction, Free Radic. Biol. Med. 107 (2017) 2–12.

[3] K.G.M.M. Alberti, R.H. Eckel, S.M. Grundy, P.Z. Zimmet, J.I. Cleeman, K.A. Donato, J.-C. Fruchart, W.P.T. James, C.M. Loria, S.C. Smith, Harmonizing the metabolic syndrome, Circulation 120 (2009) 1640–1645.

[4] J.A.S. Carson, A.H. Lichtenstein, C.A.M. Anderson, L.J. Appel, P.M. Kris-Etherton, K.A. Meyer, K. Meyer, K. Petersen, T. Polonsky, L. Van Horn, L. Van Horn, Dietary cholesterol and cardiovascular risk: a science advisory from the American heart association, Circulation 141 (2020) e39–e53.

[5] S. Castro-Barquero, A.M. Ruiz-León, M. Sierra-Pérez, R. Estruch, R. Casas, Dietary strategies for metabolic syndrome: a comprehensive review, Nutrients 12 (2020) 2983.

[6] L. Guo, S. Chen, Y.-L. Yu, J.-A. Wang, A smartphone optical device for point-of-care testing of glucose and cholesterol using Ag NPs/UiO-66-NH(2)-based ratiometric fluorescent probe, Anal. Chem. 93 (2021) 16240–16247.

[7] J.J. Samulak, A.K. Sawicka, D. Hartmane, S. Grinberga, O. Pugovics, W. Lysiak-Szydlowska, R.A. Olek, L-carnitine supplementation increases trimethylamine-N-oxide but not markers of atherosclerosis in healthy aged women, Ann. Nutr. Metab. 74 (2019) 11–17.

[8] N. Khaliq, M.A. Rasheed, G. Cha, M. Khan, S. Karim, P. Schmuki, G. Ali, Development of non-enzymatic cholesterol bio-sensor based on TiO2 nanotubes decorated with Cu2O nanoparticles, Sensor. Actuator. B Chem. 302 (2020) 127200.

[9] R. Mirzajani, F. Kardani, Z. Ramezani, A nanocomposite consisting of graphene oxide, zeolite imidazolate framework 8, and a molecularly imprinted polymer for (multiple) fiber solid phase microextraction of sterol and steroid hormones prior to their quantitation by HPLC, Microchim. Acta 186 (2019) 129.

[10] T. Xia, G. Liu, J. Wang, S. Hou, S. Hou, MXene-based enzymatic sensor for highly sensitive and selective detection of cholesterol, Biosens. Bioelectron. 183 (2021) 113243.

[11] Q. Yang, X. Wang, H. Peng, M. Arabi, J. Li, H. Xiong, J. Choo, L. Chen, Ratiometric fluorescence and colorimetry dual-mode assay based on manganese dioxide nanosheets for visual detection of alkaline phosphatase activity, Sensor. Actuator. B Chem. 302 (2020) 127176.

[12] Y. Chen, L. Jiao, R. Li, L. Hu, X. Jia, Z. Zhu, Y. Zhai, X. Lu, Immobilizing glucose oxidase on AuCu hydrogels for enhanced electrochromic biosensing, Anal. Chim. Acta 1283 (2023) 341977.

[13] Y. Liu, F. Wang, Y. Liu, L. Cao, H. Hu, X. Yao, J. Zheng, H. Liu, A label-free plasmonic nanosensor driven by horseradish peroxidase-assisted tetramethylbenzidine redox catalysis for colorimetric sensing H2O2 and cholesterol, Sensor. Actuator. B Chem. 389 (2023) 133893.

[14] R. Zhang, X. Yan, K. Fan, Nanozymes inspired by natural enzymes, Acc. Mater. Res. 2 (2021) 534–547.

[15] J. Li, T. Liu, R.A. Dahlgren, H. Ye, Q. Wang, Y. Ding, M. Gao, X. Wang, H. Wang, N, S-co-doped carbon/Co1-xS nanocomposite with dual-enzyme activities for a smartphone-based colorimetric assay of total cholesterol in human serum, Anal. Chim. Acta 1204 (2022) 339703.

[16] Y. Li, X. Gu, J. Zhao, F. Xi, Fabrication of a ratiometric fluorescence sensor based on carbon dots as both luminophores and nanozymes for the sensitive detection of hydrogen peroxide, Molecules 27 (2022) 7379.

[17] B. Shen, M. Qing, L. Zhu, Y. Wang, L. Jiang, Dual-enzyme cascade composed of chitosan coated FeS2 nanozyme and glucose oxidase for sensitive glucose detection, Molecules 28 (2023) 1357.

[18] B. Lu, Q. Liu, S. Chen, Electrocatalysis of single-atom sites: impacts of atomic coordination, ACS Catal. 10 (2020) 7584–7618.

[19] Y. Peng, B. Lu, S. Chen, Carbon-supported single atom catalysts for electrochemical energy conversion and storage, Adv. Mater. 30 (2018) 1801995.

[20] Y.X. Wang, H.Y. Su, Y.H. He, L.G. Li, S.Q. Zhu, H. Shen, P.F. Xie, X.B. Fu, G. Y. Zhou, C. Feng, D.K. Zhao, F. Xiao, X.J. Zhu, Y.C. Zeng, M.H. Shao, S.W. Chen, G. Wu, J. Zeng, C. Wang, Advanced electrocatalysts with single-metal-atom active sites, Chem. Rev. 120 (2020) 12217–12314.

[21] R. Li, W. Guo, Z. Zhu, Y. Chen, L. Jiao, C. Zhu, Y. Zhai, X. Lu, Single-site Sn-O-Cu pairs with interfacial electron transfer effect for enhanced electrochemical catalysis and sensing, Small 19 (2023) 2300149.

[22] R. Li, W. Guo, Z. Zhu, Y. Zhai, G. Wang, Z. Liu, L. Jiao, C. Zhu, X. Lu, Single-atom indium boosts electrochemical dopamine sensing, Anal. Chem. 95 (2023) 7195–7201.

[23] J. Kim, H.-E. Kim, H. Lee, Single-atom catalysts of precious metals for electrochemical reactions, ChemSusChem 11 (2018) 104–113.

[24] Y. Chen, P. Wang, H. Hao, J. Hong, H. Li, S. Ji, A. Li, R. Gao, J. Dong, X. Han, M. Liang, D. Wang, Y. Li, Thermal atomization of platinum nanoparticles into single atoms: an effective strategy for engineering high-performance nanozymes, J. Am. Chem. Soc. 143 (2021) 18643–18651.

[25] X. Chen, N. Li, K. Eckhard, L. Stoica, W. Xia, J. Assmann, M. Muhler, W. Schuhmann, Pulsed electrodeposition of Pt nanoclusters on carbon nanotubes modified carbon materials using diffusion restricting viscous electrolytes, Electrochem. Commun. 9 (2007) 1348–1354.

[26] S.H. Hsieh, M.C. Hsu, W.L. Liu, W.J. Chen, Study of Pt catalyst on graphene and its application to fuel cell, Appl. Surf. Sci. 277 (2013) 223–230.

[27] X. Li, W. Bi, L. Zhang, S. Tao, W. Chu, Q. Zhang, Y. Luo, C. Wu, Y. Xie, Single-atom Pt as Co-catalyst for enhanced photocatalytic H2 evolution, Adv. Mater. 28 (2016) 2427–2431.

[28] S. Fang, X. Zhu, X. Liu, J. Gu, W. Liu, D. Wang, W. Zhang, Y. Lin, J. Lu, S. Wei, Y. Li, T. Yao, Uncovering near-free platinum single-atom dynamics during electrochemical hydrogen evolution reaction, Nat. Commun. 11 (2020) 1029.

[29] M. Ou, S. Wan, Q. Zhong, S. Zhang, Y. Wang, Single Pt atoms deposition on g-C3N4 nanosheets for photocatalytic H2 evolution or NO oxidation under visible light, Int. J. Hydrogen Energy 42 (2017) 27043–27054.

[30] Y. Zhu, T. Wang, T. Xu, Y. Li, C. Wang, Size effect of Pt co-catalyst on photocatalytic efficiency of g-C3N4 for hydrogen evolution, Appl. Surf. Sci. 464 (2019) 36–42.

[31] Y. Li, X. Li, H. Zhang, J. Fan, Q. Xiang, Design and application of active sites in g-C3N4-based photocatalysts, J. Mater. Sci. Technol. 56 (2020) 69–88.

[32] Y. Zhang, Z. Chen, J. Li, Z. Lu, X. Wang, Self-assembled synthesis of oxygen-doped g-C3N4 nanotubes in enhancement of visible-light photocatalytic hydrogen, J. Energy Chem. 54 (2021) 36–44.

[33] Z. Mo, Z. Miao, P. Yan, P. Sun, G. Wu, X. Zhu, C. Ding, Q. Zhu, Y. Lei, H. Xu, Electronic and energy level structural engineering of graphitic carbon nitride nanotubes with B and S co-doping for photocatalytic hydrogen evolution, J. Colloid Interface Sci. 645 (2023) 525–532.

[34] Y. Yang, J. Yan, Y. Zhang, S. Xing, J. Ran, Y. Ma, X. Li, S/P co-doped g-C3N4 with secondary calcination for excellent photocatalytic performance, Int. J. Hydrogen Energy 51 (2023) 962–974.

[35] X. Dang, R. Yang, Z. Wang, S. Wu, H. Zhao, Efficient visible-light activation of molecular oxygen to produce hydrogen peroxide using P doped g-C3N4 hollow spheres, J. Mater. Chem. A 8 (2020) 22720–22727.

[36] X. Wang, X. Wang, W. Tian, A. Meng, Z. Li, S. Li, L. Wang, G. Li, High-energy ball-milling constructing P-doped g-C3N4/MoP heterojunction with Mon bond bridged interface and Schottky barrier for enhanced photocatalytic H2 evolution, Appl. Catal. B Environ. 303 (2022) 120933.

[37] S. Ding, J.A. Barr, Z. Lyu, F. Zhang, M. Wang, P. Tieu, X. Li, M.H. Engelhard, Z. Feng, S.P. Beckman, X. Pan, J.-C. Li, D. Du, Y. Lin, Adv. Mater. 36 (2024) 2209633.

[38] F. Nichols, Q. Liu, J. Sandhu, Z. Azhar, R. Cazares, R. Mercado, F. Bridges, S. Chen, Platinum-complexed phosphorous-doped carbon nitride for electrocatalytic hydrogen evolution, J. Mater. Chem. A 10 (2022) 5962–5970.

[39] B. Han, H. Guan, Y. Song, Y. Liu, Radix pueraria flavonoids assisted green synthesis of reduced gold nanoparticles for electrochemical nonenzymatic detection of cholesterol in food samples, ACS Omega 7 (2022) 43045–43054.

[40] J. Sun, B. Xu, Y. Mu, H. Ma, W. Qu, Functional magnetic nanoparticles for highly efficient cholesterol removal, J. Food Sci. 83 (2018) 122–128.

[41] Y. Peng, B. Lu, L. Chen, N. Wang, J.E. Lu, Y. Ping, S. Chen, Hydrogen evolution reaction catalyzed by ruthenium ion-complexed graphitic carbon nitride nanosheets, J. Mater. Chem. A 5 (2017) 18261–18269.

[42] Y. Peng, W. Pan, N. Wang, J.-E. Lu, S. Chen, Ruthenium ion-complexed graphitic carbon nitride nanosheets supported on reduced graphene oxide as high-performance catalysts for electrochemical hydrogen evolution, ChemSusChem 11 (2018) 130–136.

[43] Z. Wang, X. Ren, X. Shi, Abdullah M. Asiri, L. Wang, X. Li, X. Sun, Q. Zhang, H. Wang, A platinum oxide decorated amorphous cobalt oxide hydroxide nanosheet array towards alkaline hydrogen evolution, J. Mater. Chem. A 6 (2018) 3864–3868.

[44] S.C. Yan, Z.S. Li, Z.G. Zou, Photodegradation of rhodamine B and methyl orange over boron-doped g-C3N4 under visible light irradiation, Langmuir 26 (2010) 3894–3901.

[45] M. Sarno, E. Ponticorvo, Much enhanced electrocatalysis of Pt/PtO2 and low platinum loading Pt/PtO2-Fe3O4 dumbbell nanoparticles, Int. J. Hydrogen Energy 42 (2017) 23631–23638.

[46] H. Wu, Z. Chen, Y. Wang, E. Cao, F. Xiao, S. Chen, S. Du, Y. Wu, Z. Ren, Regulating the allocation of N and P in codoped graphene via supramolecular control to remarkably boost hydrogen evolution, Energy Environ. Sci. 12 (2019) 2697–2705.

[47] D.T. Clark, D. Briggs, D.B. Adams, ESCA studies of square-planar platinum complexes; correlations with nuclear quadrupole resonance studies, J. Chem. Soc. Dalton Trans. (1973) 169–172.